Coastline Extraction and Change Analysis from Satellite Data - 2015 –2022

Report

May 2023

Contacts

Brockmann Consult:

Kerstin Stelzer

Email: kerstin.stelzer@brockmann-consult.de

Tel: +49(0)40 696 389 307

Brockmann Geomatics:

Petra Philipson

Email: petra.philipson@brockmann-geomatics.se

Tel: 070 699 60 46

Statens Geotekniska Institut (SGI):

Sebastian Bokhari Irminger

Email: sebastian.bokhari-irminger@sgi.se

Tel: 040 35 67 71

Authors:

Kerstin Stelzer (BC)

Petra Philipson (BG)

CONTENT

Sammanfattning

Rapporten är en sammanfattning av ett antal utvecklings- och tillämpningsuppdrag som huvudsakligen genomfördes under 2022 för SGIs räkning. Ursprunget till uppdragen är ett tidigare arbete för SGI av Brockmann som visade på fjärranalysens potential för kustzonsförvaltning för ett flertal tillämpningar (Philipson et al. 2021). I det arbetet beskrevs bland annat potentialen för kustlinjekartering baserat på Sentinel-2 data. Resultaten bedömdes som lovande av SGI, men att ytterligare analys kring hur övergången mellan land och vatten ska identifieras krävdes för att öka metodens träffsäkerhet och användbarhet.

Den första delen av uppdraget omfattade alltså fortsatt utveckling av användandet av ett eller flera index för att identifiera kustlinjen. Målet var att metoden ska kunna hantera varierande geologiska förhållanden såsom stenstränder, sandstränder, och varierande förekomst av flytande eller fast vattenvegetation i de grundaste områdena. Det gjordes även ett antal tester med avseende på formatet för den efterföljande förändringsanalysen baserat på de identifierade kustlinjerna.

Efter utvecklingsfasen tillämpades metoden på samtliga Sentinel-2-bilder registrerade mellan 2015 och 2022 över Ystad kommun, Helsingborg och Laholmsbukten. Resultatet inkluderade identifiering av strandlinjen samt en förändringsanalys för transekter vinkelrätta mot kustlinjerna med 100 meters avstånd.

Summary

The report is a summary of several development and application assignments that were mainly carried out during 2022 on behalf of SGI. The origin of the assignments is a previous work for SGI by Brockmann, which showed the potential of remote sensing for coastal zone management for several applications (Philipson et al. 2021). In that work, among other things, the potential for coastline mapping based on Sentinel-2 data was described. The results were assessed as promising by SGI, but that further analysis of how the transition between land and water should be identified was required to increase the accuracy and usability of the method.

The first part of the assignment therefore included continued development of the use of one or more indexes to identify the coastline. The goal was that the method should be able to handle varying geological conditions such as rocky beaches, sandy beaches, and varying occurrence of floating or attached water vegetation in the shallowest areas. Several tests were also made regarding the format of the subsequent change analysis based on the identified coastlines.

After the development phase, the method was applied to all Sentinel-2 images registered between 2015 and 2022 over Ystad municipality, Helsingborg and Laholmsbukten. The result included identification of the shoreline as well as a change analysis for transects perpendicular to the coastlines with 100 meters distance.

1 Introduction

Within a study performed in 2021, several coastal products derived from satellite data were presented to SGI. Coastline detection and the coastline change was one of the topics raising high interest. Coastlines are derived from spectral band indices which behave differently for water and for land surface types, and different indices perform differently for different (coastal) surface types. The delivered test products from the above mentioned study performed well for most of the coastal environments, especially for sandy beaches. But they also showed discrepancies for other geological areas, such as very narrow beaches, beaches with macro algae in shallow waters, stony coastal protection constructions.

The municipality of Ystad was selected as study area to further evaluate the accuracy of the coastlines derived from Sentinel-2 data and to find a good solution for different coastal environments.

In detail, the following questions were raised and discussed in this report:

- How to select the most suitable index for Ystad coastline?
- Is a separation of the coastline into several sub-sections suitable and useful?
- How does the geolocation accuracy influence the coastline extraction?
- What is the accuracy of a derived coastline along the Ystad coastline?

In the second phase, after successfully answering the above questions, the shorelines for all suitable satellite acquisitions between 2016 and 2021 were extracted and a shoreline change analyses was performed.

This report provides the information about the selected algorithms to derive the shorelines from satellited data and the accuracy of the applied approach (phase 1) and it provides an overview of the processed data for the longer time series and derived results of shoreline change detection (phase 2). This report comes with the delivery of several shapefiles containing the shoreline extractions and the shoreline change analysis statistics.

A supplement to the 2 phases has been added in September 2022. This third delivery included the coastline extraction for 2015 and 2022. In addition, the distances of transects were reduced to 100m.

2 Algorithms

2.1 Coastline Extraction

2.1.1 Land-Water Indices

Shoreline positions can be delineated manually from satellite images, but this process is inefficient, and the accuracy depends on the experience of the operator (Apostolopoulos and Nikolakopoulos, 2021). For this reason, various different methods have been developed to

automize this process over the last decades (Toure et al., 2019). Among the approaches which have successfully been applied for land-sea segmentation are, for instance, Principal Component Analysis (PCA), K-means and ISODATA clustering or complex neural networks. A rather simple approach which has been used for decades, are band ratio or index thresholding that increase the contrast between land and water. They take advantage of the low reflectance of water in the Near Infrared (NIR) and/or in the Short-Wave Infrared (SWIR) compared to most land surfaces and have proven to be as reliable as machine learning approaches (Li et al. 2022).

Within this study, we tested different spectral indices along the shoreline of Ystad Municipality and assessed their performance for the different coastal shapes and material. It was also investigated if the detection of the shoreline improves when the shoreline is separated in natural sections in order to optimize the thresholding of the respective indices. The tests showed that a modified version of the Normalized Difference Water Index (NDWI; McFeeters 1996) performed best along the coasts of Ystad municipality. The index is derived by a combination of the blue and the near Infrared band:

$$NBNI = \frac{Blue - NIR}{Blue + NIR}$$

The difference between the original NDWI and the Normalized Blue Nir Index (NBNI) is that the Green band is replaced by the Blue band, which increases the contrast between the relatively dark Baltic Sea and the different shore types. The NBNI is particularly suited for Sentinel-2 MSI as it exploits the highest possible spatial resolution of the sensors. Both Blue and NIR bands are sampled in the finest spatial resolution (10 m).

However, NBNI has problems to supress effects of certain surface types in urban environments. In such regions, the Automated Water Extraction Index for non-shadow surfaces (AWEI; Feyisa et al. 2014) performs significantly better:

$$AWEI = 4 \cdot (Green - SWIR1) - (0.25 \cdot NIR + 2.75 \cdot SWIR2)$$

By including both short-wave infrared (SWIR) bands, non-water low albedo surfaces can be differentiated from water. However, the pixel resolution of Sentinel-2 MSI in these bands is 20 m and therefore a resampling of the SWIR bands to the higher resolution of the green band is necessary for further processing. Bilinear interpolation was used for this task.

2.1.2 From Index to Coastline

The water indices discussed in the previous section provide a raster of index values. In the case of NBNI, the normalized form of the equation constraints values to the range from -1 to 1, whereas AWEI can produce larger values. In both cases, they will vary around zero. Positive values indicate water, while negative values are associated with land surfaces. From a theoretical point of view, a fixed threshold of 0 can be used to divide the image into the two classes (McFeeters, 1996). However, several studies have shown that the classification is more accurate, if the threshold is adapted to the local brightness and contrast conditions of the surface environment and the atmosphere (Feyisa et al., 2014; Toure et al., 2019; Bishop-Taylor et al., 2019). Different global image thresholding algorithms can automate this process. We deployed Otsu's algorithm, which finds the threshold that maximises the variance between the classes (i.e. water and land) in the

bi-modal distribution and minimizes the variance within both classes. Several studies have shown excellent results of this algorithm in the context of shoreline detection (e.g. Bishop-Tylor et al. 2019, Sekertekin 2021).

For this study, we investigated both - a fixed threshold as well as the Otsu derived thresholds for different geological subsections of Ystad coastline. The best result was derived by the Otsu derived thresholds applied to five sub-sections (see below).

Water index and Otsu thresholding yield a “water” – “land” raster image. Along the coastline are pixels, which are partly water and partly land. To account for these mixed pixels, the marching-squares algorithm has been applied, which considers the water index values of the vicinity around each pixel to linearly interpolate the border between water and land (Cipolletti et al. 2012). With this method, it is possible to locate the position of the shoreline at sub-pixel precision (Vos et al. 2019).

2.1.3 Identification of regional subsections and merging at transition zones

Coasts consists of several different types, including sandy beaches, cliffs, stony beaches with large boulders in the foreshore, vegetated coast and manmade structures such as harbours and groins. Due to the strong differences in reflectance characteristics of e.g. bright sandy beaches and relatively dark rocky shores, the optimal threshold between water and land may vary for a study area. For this reason, a shoreline can be split into several sections and analysed separately. For Ystad, a test was performed to separate the coast into five different areas: The area west of Ystad, which mainly consist of rocky beaches and vegetated shorelines with few sandy beaches, the harbour of Ystad, the sandy beach between Ystad and Margretevall, the rocky coast between Kåseberga and Löderups Strandbad and the bright beach of Sandhammaren further east (Figure 1). It has already been mentioned that NBNI performs well along “natural” parts of the coast, whereas shorelines in urban areas are subject to false classifications of certain surface types. For this reason, shorelines at the harbour of Ystad were delineated with AWEI, whereas NBNI was deployed along the other parts of the coast of Ystad municipality.

Figure 1: The five processing tiles along the coast of Ystad municipality. Background image is a true color rendering of Sentinel-2B MSI from 2021-07-20.

Within each subsection, separate thresholds were calculated with Otsu’s algorithm, which adapts to the local brightness conditions. However, this procedure yields unconnected pieces of the

shoreline, which therefore have to be merged. To solve this, adjacent tiles, and thus also the derived shorelines, were generated with an overlap of approximately 100 m. The individual shoreline segments were then smoothly connected with a dynamic segmentation approach: both overlapping shoreline parts are divided into 100 points. Next, the (linearly) weighted average between the coordinates of two corresponding points is calculated. Connecting the average positions smoothly blends from one shoreline segment to the segment in the adjacent tile (Figure 2). In the transition areas between the different tiles, only the merged shoreline is retained. With this procedure, a single continuous shoreline along the whole coast of Ystad municipality could be produced, henceforth called Satellite Derived Shoreline, SDS.

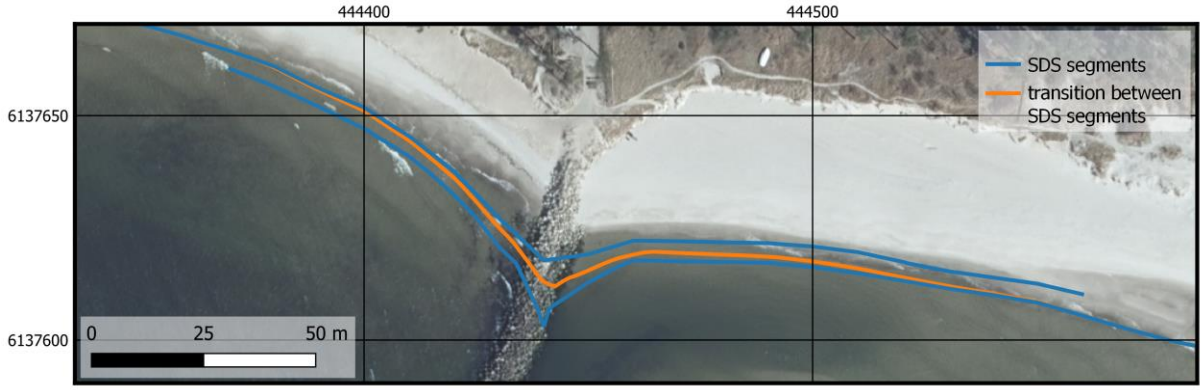

Figure 2: Illustration of the smooth transition between different segments of the satellite derived shoreline (SDS).

2.1.4 Improvement of Geolocation of input satellite data

A major source of SDS positional uncertainty is georeferencing errors of the satellite sensors. For Sentinel-2, the long-term absolute geolocation uncertainty is appr. 11 m (95 % circular error; ESA, 2022). The introduction of a new Global Reference Image (GRI) in August 2021 reduced the errors to appr. 6 m. The full archive of data will be reprocessed with the new baseline and become available around mid-2023. Until then, some Sentinel-2 scenes are subject to significant mis-registrations which impair the quality of SDS.

Therefore, we tested the ability of the Automated and Robust Open-Source Image Co-Registration Software (AROSICS, version 1.7.6) to reduce georeferencing errors. AROSICS estimates the displacement between two images using phase correlation based on a single band (red band) in a subset of the images (global co-registration; Scheffler et al., 2017). It is robust against different atmospheric conditions, changes of land cover and illumination geometries. All satellite scenes were co-registered with the Sentinel-2 B MSI scene from 20.07.2021 as reference. This scene has been geolocated with the new GRI and a visual inspection proved a high agreement between this scene and reference orthophotos.

2.1.5 Validation of the satellite derived coastline against high-resolution orthophotos

To quantify the accuracy of our approach, offsets between SDS and reference shorelines were calculated. Reference shorelines were manually digitized at the land-water boundary in high-resolution orthophotos provided by the Swedish Land Survey. Since the launch of the first Sentinel-2, three orthophotos were acquired (2016, 2018, 2020). Unfortunately, the 2018 orthophoto has been made during a period with a relatively low water level, which hinders a comparison with SDS derived at mean water levels. For this reason, only the reference shorelines from 2016 and 2020 were used for validation.

SDS were derived from satellite scenes close to the acquisition date of the orthophotos (± 3 weeks). This ensures that morphological changes of the coast between the two images are small. For both reference shorelines, four almost cloud free scenes were identified (Table). To estimate the effect of additional co-registration on SDS accuracy, SDS were delineated with and without co-registration.

Table 1: Reference and Sentinel-2 data used for validation

Orthophoto date	Sentinel-2 date	Days difference
12.-13.05.2016	02.05.2016	10
	09.05.2016	-3
	12.05.2016	0
	21.05.2016	8
03.06.2020	21.05.2020	-13
	31.05.2020	-3
	07.06.2020	4
	25.06.2020	22

Distances between reference shorelines and each SDS were derived using the Directional Buffer Overlay method (DBO; extension of Heo et al. 2009), which uses transects to separate the coast into smaller zones of about 100 m width. Within each of the zones, the average distance between the two lines is derived by creating a small buffer of 1 m width around the reference shoreline. The length of the SDS within the buffer is calculated and stored. Next, the buffer distance is increased by one meter and the process is repeated, until the buffer does not include any part of the SDS. The average distance between the lines is estimated from the distance distribution by calculating the weighted average.

The Mean Absolute Error (MAE) has been calculated to estimate the average distance between SDS and reference shoreline. It must be noted that the zones between consecutive transects do not have a constant size, as the shoreline continuously bends. For this reason, the derived offsets

in each zone were weighted according to the size of the corresponding zone when calculating the MAE.

$$MAE = \frac{1}{\sum w}\sum_{i=1}^{n} w_i \times \left||o_i|\right|$$

where o_i is the offset between reference shoreline and SDS in the $i-$ th zone and w_i is the area of this zone.

Systematic offsets of SDS are estimated with the (area-weighted) bias:

$$bias = \frac{1}{\sum w}\sum_{i=1}^{n} w_i \times o_i$$

where negative/positive values indicate a landward/seaward offset of the SDS.

The standard deviation (std) of the errors is used to assess how closely the SDS follows the shape of the reference shoreline, even if it is systematically offset:

$$std = \sqrt{\left(\frac{1}{\sum w}\sum_{i=1}^{n} w_i \times o_i - bias\right)^2}$$

2.2 Shoreline Change

After extraction of all shorelines, the change analysis was conducted and statistical measures were calculated. Shoreline change is mainly expressed with four measures, which are also the core analytics in the tools AMBUR and DSAS (Jackson et al., 2012; Himmelstoss et al., 2021): Net shoreline movement (NSM), shoreline change envelope (SCE), end point rate (EPR) and linear regression rate (LRR).

NSM is defined as the distance between the first and the latest shoreline measurement along a transect and thus quantifies the net effect of shoreline change (Khallaghi and Pontius, 2021). Changes that occurred between the start and end of the observational period are not considered by this metric, but it serves as an indicator for magnitude and direction of net shoreline change.

SCE is the total distance between the most seaward and most landward shorelines and quantifies the overall dynamics of the shoreline along the transects. This measure is sensitive to outliers of shorelines, e.g. from acquisitions during very low or high water level or undetected errors caused by haze.

EPR divides the NSM by the time between first and last shoreline.

LRR is the slope of the fitted linear model to the time-dependent shoreline positions, where the slope of regression is the rate of trend (LRR) (Burningham and Fernandez-Nunez, 2020).

All above listed indicators have been calculated for all transects perpendicular to the shorelines. The transects were derived by an automated method that first defines one outer and one inner baseline by generating a buffer around all extracted shorelines and then performs a subsequent smoothing. The starting point of each transect are then positioned with a user defined distance along the outer baseline. The end point of each transect is then defined as the point where the transect meets the inner baseline and the position of a shoreline is determined as the distance to the landside baseline along the transect.

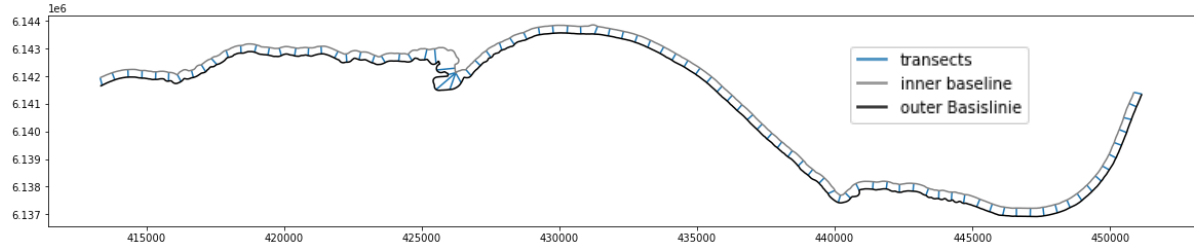

Figure 3. Baselines and transects along the coastline of municipality of Ystad.

3 Validation Results

3.1 Accuracy of generated Coastlines

Figure 4 shows two sections of the Ystad coast and the derived coastlines from satellite acquisitions that were close to the acquisition of the orthophoto in 2016 (upper panel) and 2020 (lower panel). The background image is the orthophoto acquired on 12th and 13th May and on 3rd June 2020. Not much change is expected during this three week period and the derived coastlines show very good agreement. Only the coastlines in the second example of 2020 (Löderup, Figure 4D) shows larger differences. We investigated if this is due to real change of the beach or if it is a failure of the coastline detection. The results showed that in fact, the shape of the beach was changing within this period and that the coastlines are captured well from the satellite data.

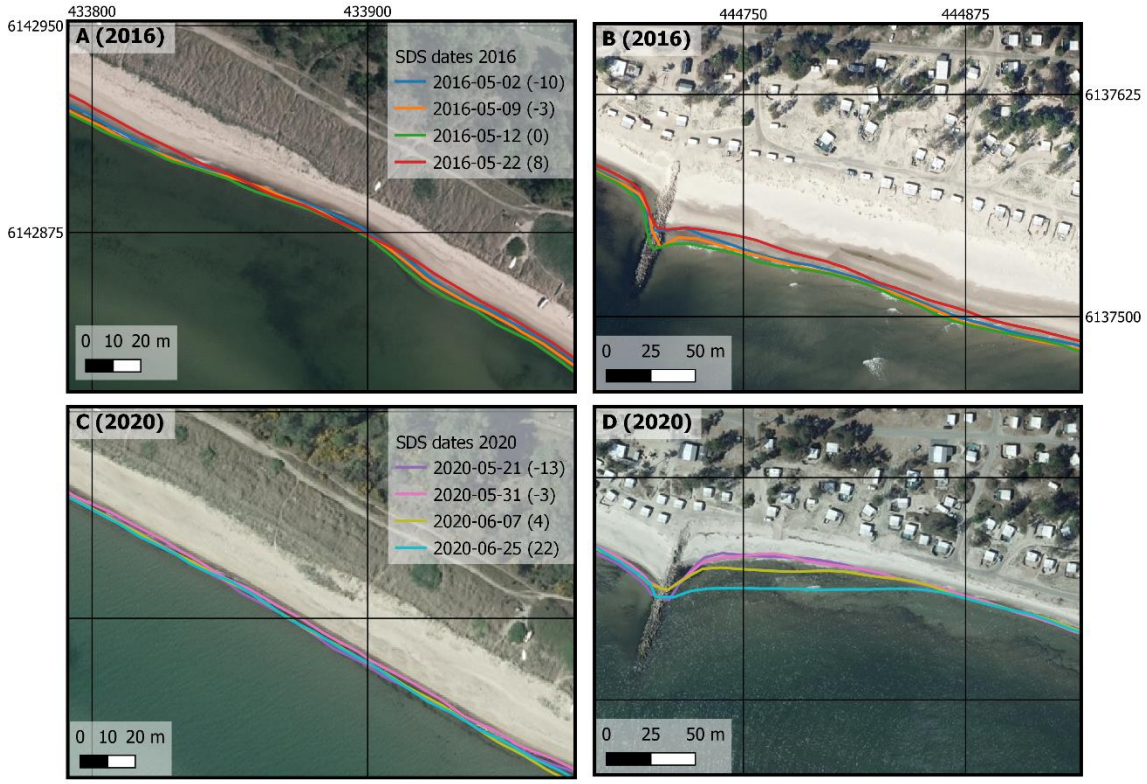

Figure 4: Example of derived coastlines with short time differences for 2016 (above) and 2020 (below) for two different coastal areas. Numbers in brackets after the date of the satellite acquisition indicates the number of days before (-) and after the acquisition of the orthophoto.

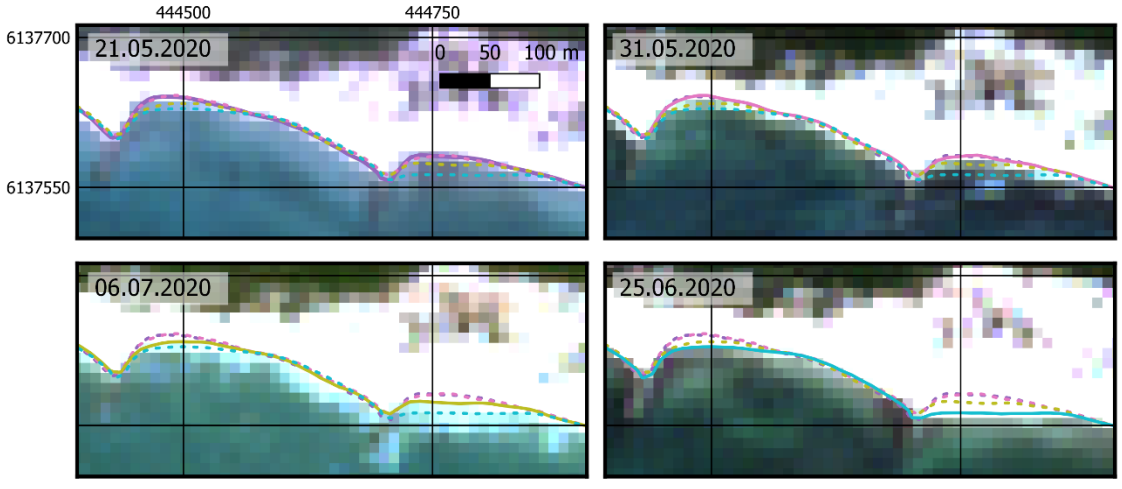

Figure 5: Satellite images and derived coastlines from 2020 showing the potential change of the beach within the three-weeks period (Figure 4D)

Table Table 2 shows the statistical results of the validation. Without co-registration, MAE ranges between 3.6 and 11 m with an average of 6.4 m. Additional co-registration reduces average errors by more than 2 m to 4.2 m MAE. Moreover, errors are more constant and range between 3.1 and 5.0 m. The same applies to bias and std, which are 1.2 m (i.e. slight seaward offset) and 6.6 m, respectively.

Table 2 Error statistics of SDS comapred to the reference shorelines.

date	No co-registration			Co-registered		
	MAE [m]	Bias [m]	std [m]	MAE [m]	Bias [m]	std[m]
02.05.2016	7.5	4.4	10.3	4.1	-0.1	7.8
09.05.2016	7.1	-3.8	8.0	4.3	2.2	5.8
12.05.2016	7.3	5.5	6.8	4.5	2.3	6.3
22.05.2016	4.3	0.4	7.9	4.1	-1.8	6.9
21.05.2020	3.6	-0.6	5.3	3.8	1.6	5.3
31.05.2020	3.7	1.2	6.2	3.1	-0.5	5.7
07.06.2020	6.6	4.5	8.1	4.5	2.3	7.0
25.06.2020	11	8.8	9.9	5.0	3.6	6.0
average	**6.4**	**2.6**	**8.8**	**4.2**	**1.2**	**6.6**

The accuracy of shorelines derived with the presented method reaches sub-pixel precision as it is higher than the finest pixel resolution of Sentinel-2 (10 m). Moreover, our approach performs better than, to our best knowledge, any published methods. For instance, Hagenaars et al. (2018) reached an average offset of 9.5 m and a std of 12 m in a case study at a beach in the Netherlands, whereas Vos et al. (2019) reported a bias of 1.2 m and an RMSE (equivalent to the std in this study) of about 8 m in a validation at five beaches around the world. Costantina et al. (2020) reached biases of 4.5, -5.2 and 8.7 and stds of 9.4, 8.2 and 6.4 m along three stretches of the Italian coast.

Figure 6 clearly shows that errors are not randomly distributed across the study area. Error hotspots include the coast west of Ystad, the harbour of Ystad, parts of the cliffs south of Kåseberga and the beach of Sandhammaren.

Figure 6: Spatial distribution of MAE for the co-registered SDS along the coast of Ystad municipality. Yellow boxes in A show the positions of subsets B and C. B: Differences of MAE at the sandy and rocky parts of the beach near Svarte. C: MAE south of Kåseberga. Background image in A is the Sentinel-2 MSI RGB from 20.07.2021, whereas the orthophoto from 2020 provided by Swedish Land Survey was used as background in B and C.

The shoreline west of Ystad is characterized by a frequent change of the coastal type. For beaches, rocky and densely vegetated coasts, the optimal threshold between water and land differs. This results in coastal type-dependent offsets of the SDS. For instance, in Figure 6b, MAE is smaller at the beach, whereas at the rocky part of the coast, the coastline is usually offset seawards by several meters. As the different coastal types are in a close succession, they were grouped in one tile during the shoreline generation in order to prevent that regions get too small for a reliable estimation of the threshold. Another source of errors at the rocky parts of the coast, are irregular observations of rocks in the foreshore related to water level fluctuations. This also explains the local error hotspot south of Kåseberga (Figure 6c), which relates well to a zone of shallow water depths. In such areas, the land-water boundary strongly depends on the water level. Different water levels at acquisition times of the orthophoto and satellite overpass may thus explain parts of the errors in these regions.

Elevated MAEs in the harbour of Ystad can be related to observations of ferries and boats, which are identified by our algorithms as land. Compared to the reference shoreline, the SDS are offset seawards where a ship is berthed.

At Sandhammaren, both relatively low and high MAEs can be observed. The periodicity indicates that this is no systematic error, but rather related to uncertainties to define “the” shoreline in both satellite image and orthophoto. Our algorithms identify the boundary between land and

water. At beaches with a low beach face slope, the position of this boundary is subject to short-term fluctuations on the order of several meters caused by wave run-up (Castelle et al. 2021). It is thus likely that parts of the errors visible in Figure 6 are related to the fact that the run-up state at orthophoto acquisition and satellite overpass are not the same. Additionally, the maximum run-up depends on the wave height and thus on meteorological conditions, which may differ between the different acquisition dates.

3.2 Known issues

With the help of the marching squares algorithm, SDS achieve a sub-pixel precision. However, Sentinel-2 MSI's resolution of 10 m limits the ability to identify small and thin coastal constructions such as groins or piers. An example is provided in Figure 2, where both SDS indicate the position of the groin with a tip to the south but fail to accurately map its course. However, most of such structures are man-made, constant in their position and therefore potentially of limited interest in the context of shoreline monitoring.

Figure 7 illustrates the influence of fluctuating water levels on shoreline position at a shallow part of the coast close to Lillesko, directly west of Ystad. The results have also shown problems of SDS accuracy caused by wave run-up during on-shore wind conditions at beaches. This area also shows rocks that are only partly water covered and influence the signal towards land signal, and which are more or less exposed depending on the water level. This effect is enforced by macroalgae growing in shallow waters. Macro algae may cause errors in the coastline even if the water level is not extremely low. The advantage of satellite data is the relatively high number of data sets acquired during different conditions. Increasing the numbers of observations reduces the stochastic effect of water level and wave run-up at acquisition time of an individual scene and improves confidence in derived products such as change statistics.

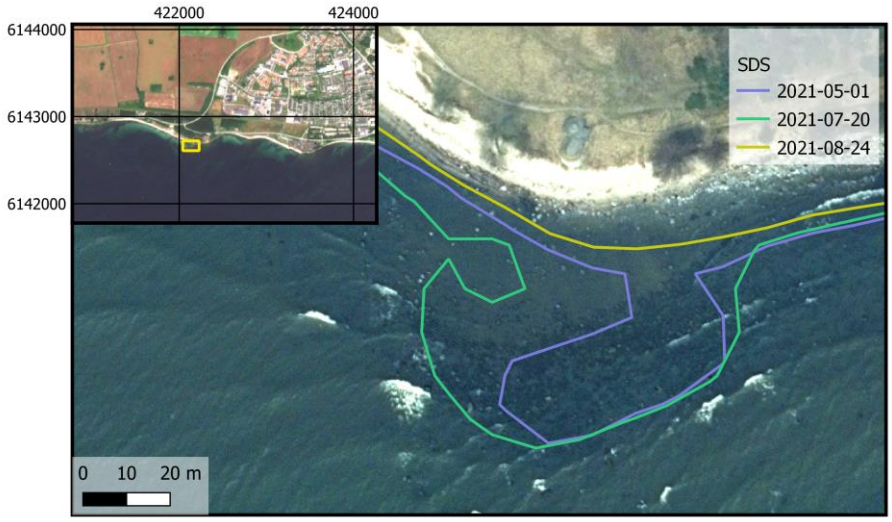

Figure 7 SDS of three different dates close to Lillesko, west of Ystad. The images were likely acquired at different water levels. Background image is an orthophoto from 13.04.2018, which was taken during a low water level.

Figure 8: Extracted coastline in Halmstad (Laholmsbukten) for a satellite acquisition during low waters (red line in the left image). The corresponding Sentinel-2 image (right side) shows dry fallen sandy areas (pink) outside the beach areas.

Moreover, if water level and wave data are available, observations with unusual environmental conditions, which do not represent the mean state of the coastal system, can be excluded from the dataset.

The influence of ships and shadows of buildings in harbour areas often cause artefacts in the derived coastlines. Figure 9 shows an example from Ystad harbour, in which the coastlines change depending on if ships are present or not. The artefacts retrieved for harbour areas led to the decision to exclude harbour areas from the data sets. Either directly in the extracted shorelines or at least for the change detection as they are not representing real changes. This decision was supported by the fact that the changes of artificial coastlines are not the main interest for the coastal erosion investigations.

Figure 9: Influence of ships in harbours on the extraction of coastlines.

Additional tests have also shown problems of SDS accuracy in low illumination conditions during winter. Shadows cause coastlines that are shifted towards the land as the shadowed areas are seen as water by the indices. Figure 10 shows an example in Laholmsbukten. These parts were excluded from the final data set to avoid a bias in coastline change estimation.

Figure 10: Shadows caused by elevated coasts in winter months (Area: west of Kattvik, Laholmsbukten)

The number of observations is lower along the coast west of Ystad, which is covered by only one orbit of Sentinel-2. The revisit time of five days limits the number of usable shoreline observations (4 in 2021) more than in the eastern part of the study area, which is covered by two orbits and is thus sensed every two to three days.

4 Shoreline extraction

4.1 Ystad

According to above findings, the shorelines at the harbour of Ystad were delineated with AWEI, whereas NBNI was deployed along the other parts of the coast of Ystad municipality. This approach was applied to all suitable Sentinel-2 images. In order to increase the number of acquisitions, the area was divided into 5 different sub-regions according to Figure 1. For each acquisition, the regions with good retrieval conditions were specified. The information about the processed region is stored in the attribute table of the vectorfiles of the derived shorelines.

DATE	REGIONS
2016-05-02T10:20:27	('W Ystad', 'Ystad', 'E Ystad', 'kaseberga', 'Sandhammae')
2016-05-09T10:10:30	('W Ystad', 'Ystad', 'E Ystad', 'kaseberga', 'Sandhammae')
2016-05-12T10:20:29	('Ystad', 'E Ystad', 'kaseberga', 'Sandhammae')
2016-05-22T10:20:29	('W Ystad', 'Ystad', 'E Ystad', 'kaseberga', 'Sandhammae')
2016-07-21T10:20:59	('W Ystad', 'Ystad', 'E Ystad', 'kaseberga', 'Sandhammae')
…	

In total, the shorelines from 133 Sentinel-2 acquisitions were extracted, while the number of valid shorelines differs from region to region due to the individual selection per region. No regions hold the shorelines from all acquisitions, so that the number of acquisitions per region is slightly lower as it is shown in Figure 11. Here, it needs to be noted that "WYstad" is covered fully only 42 times out of 103 overpasses, because the western part of this sub-region is not covered by all orbits.

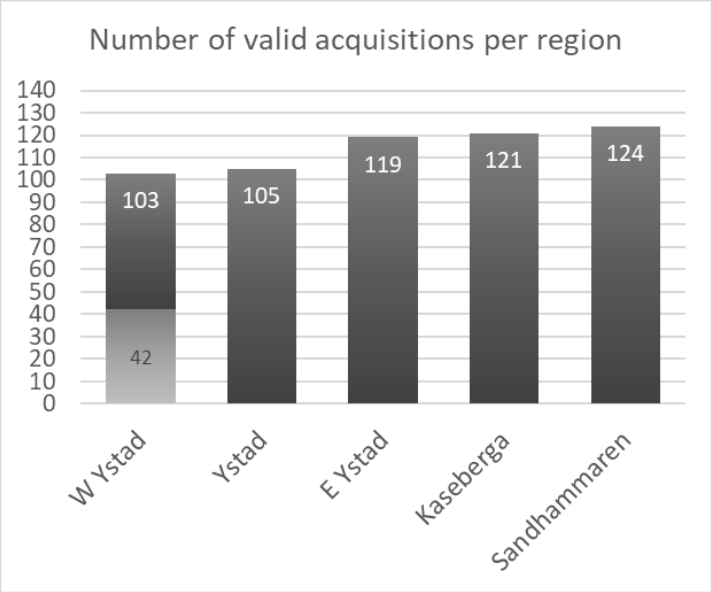

Figure 11: Number of valid sentinel-2 images per sub-region.

For a few shorelines, a manual cleaning was performed, as they were affected by small or thin clouds. In order not to lose them for the full sub-regions, the affected parts were removed from the shoreline data set.

The final shoreline data set is depicted in Figure 12, which shows the extracted coastlines along the full extent of the Ystad area as well as three examples of more detailed subsets. The date of each coastline is following the colour scheme at the right. Dark, violet lines are from 2016, while bright yellow lines are derived for satellite acquisitions in 2021.

In the subsequent figures, more detailed examples are shown comparing the extracted shoreline from all acquisitions with the orthophoto 2016 and 2020, respectively. The colours of the shorelines follow the same colour scheme as in Figure 12. However, the best way to look at the data is in a GIS system with the delivered shapefiles. The examples show areas of accretion and erosion, shifts in river inflow and the construction work in Ystad harbour during this period.

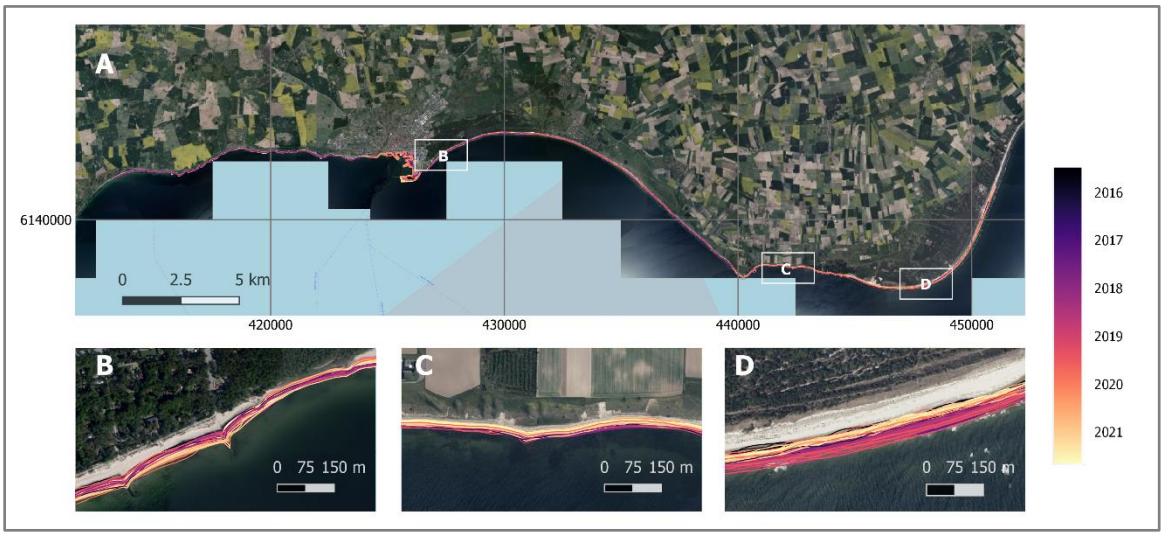

Figure 12: Maps showing the extracted coastlines for the years 2016-2021 for the whole municipality (A), as well as three subsets as examples of accretion (B) and erosion (C, D) areas. The background image is the orthophoto from 2016.

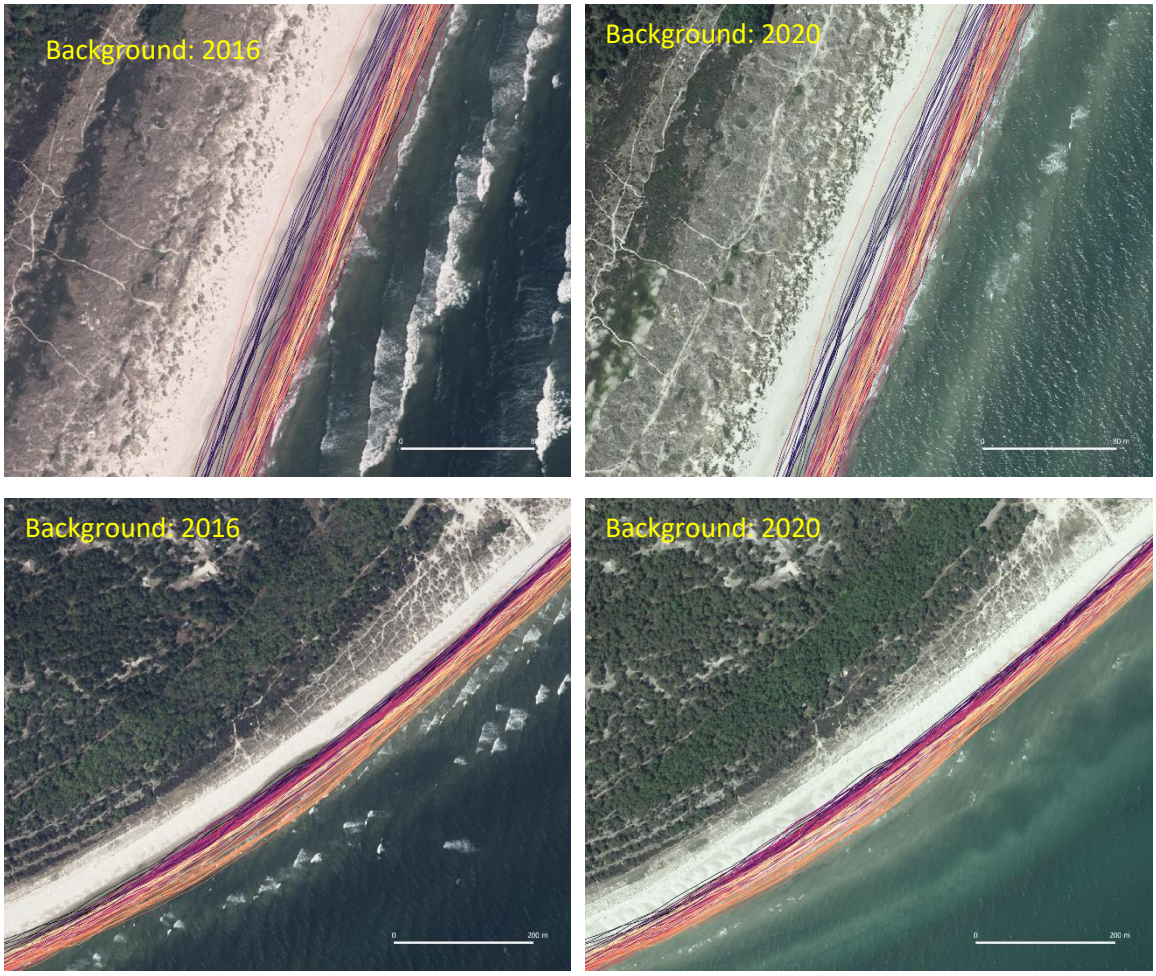

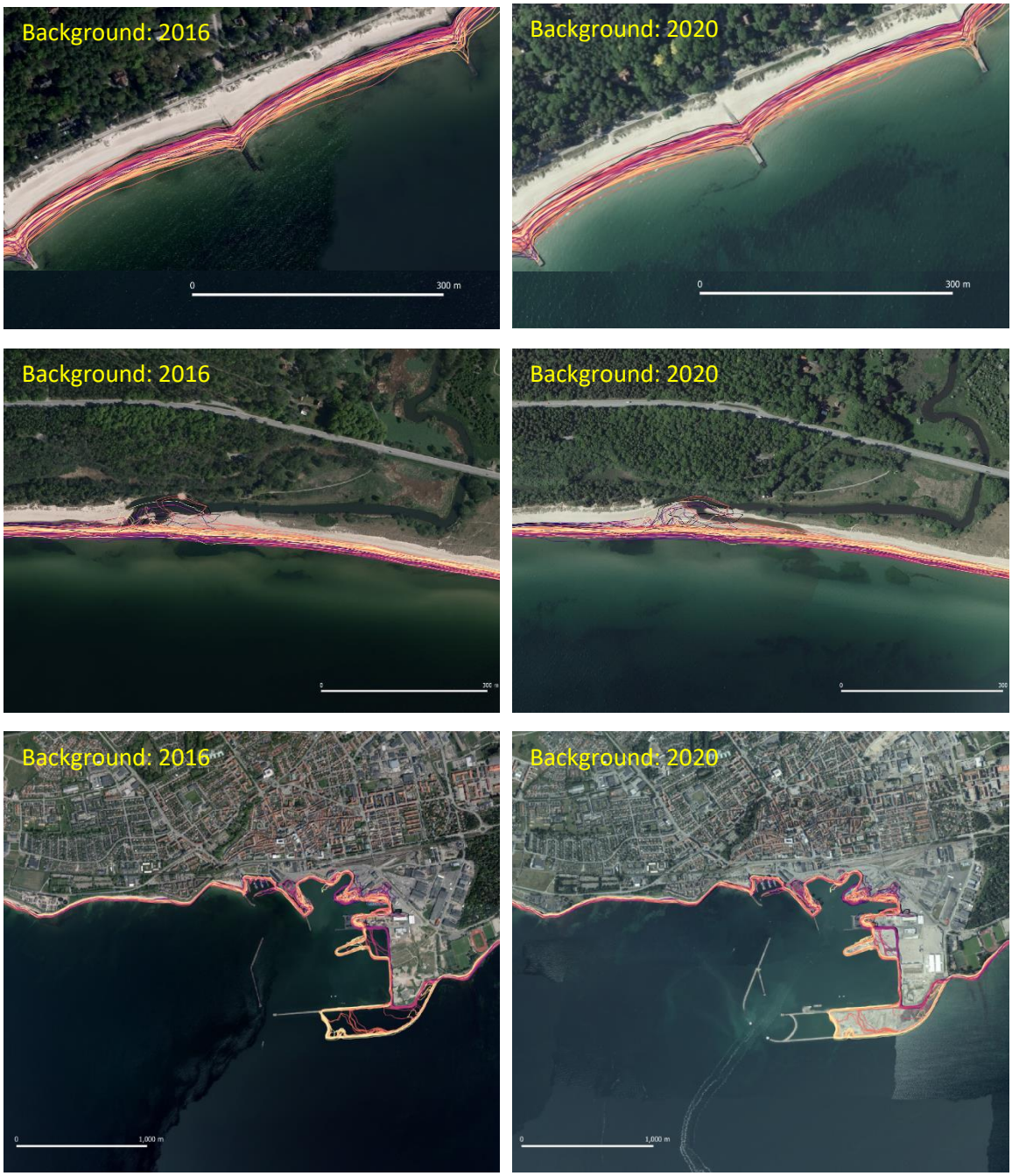

Figure 13: Examples of detailed subsets showing the extracted shorelines from all years at different locations. The left images show the shorelines overlaying the orthophoto acquired in 2016, while the images on the right show the shorelines overlaying the orthophoto acquired in 2020.

4.2 Helsingborg

For Helsingborg, the area was initially divided into four regions (Helsingborg north, Helsingborg_south, Helsingborg_centre, Helsingborg harbour). Similar as for Ystad, the NBNI was applied to all areas except the harbour region. However, for the harbour area none of the

indicators turned out to work well enough. Therefore, the section corresponding to the harbour was cut from the derived coastlines afterwards.

Figure 15 and Figure 14 show two subsets of the area north and south of Helsingborg harbour. Especially in the northern part, it occurs that the coastline is influenced by low water and macro algae growing in shallow waters (Figure 14). This effect is most dominant in May and June 2018, but also occurs in other years and months.

Figure 14: Shorelines 2015-2022 for Helsingborg north of the harbour area. Background image: Orthophoto 2020

Figure 15: Shorelines 2015-2022 for Helsingborg south of the harbour area. Background image: Orthophoto 2020

4.3 Laholmsbukten

Laholmsbukten was the largest of the three areas for which the shorelines were extracted. Figure 16 is showing the extracted shorelines of the full area. The full region was processed with the NBNI indicator and no further separation of coastal parts were conducted. The harbour area is kept in the shoreline data set but is not included in the shoreline change analysis.

Figure 16: Shoreline extraction Area Laholmbukten 2015 – 2022

Low water levels in some areas of Laholmsbukten can shift the coastlines towards the water. The false colour images of the respective acquisitions demonstrate that in those cases sediment areas seem to be dry fallen. This is visible in Figure 17 in the left image, where pink areas in the foreshore indicate dry fallen areas. The image at the right shows the extracted shoreline for that day in red (15.04.2019). Those lines were kept in the data set as they show the shoreline at that day during the time of acquisition.

Figure 17: shoreline position for low water level (acquisition 15.04.2019)

Special cases for Laholmsbukten, which have been corrected in a subsequent manual step were coastline acquired during strong winds and for which the NBNI was influenced by waves and white caps as well as shadowed areas in winter months (see Helsingborg section). Those lines were erased from the data set. Also, the area of the harbour is excluded from the data set.

Figure 18: Acquisition during strong winds (left, RGB S2 image) leads to wrong shoreline extraction (red line in the right image)

5 Shoreline Change Detection

When reliable coastlines have been derived, the shoreline change can be calculated. This step was performed as described Ch. 2.2. In the final delivery, transects generated perpendicular to the baseline and with a distance of 100 m was used to calculate the shoreline change.

5.1 Ystad

For Ystad, two versions of change detection were delivered. The first one covering 2016-2021, the second 2015-2022. The following description relates to the first delivery, but is transferable to the second delivery as well. However, in the second delivery, the change detection was not conducted for the harbour region as the influence of shadowing buildings and ships at the landing stages were too strong and caused to many artefacts in the coastlines. Besides this, the following observations are true to both versions.

The area between Löderups strandbad and Sandhammaren havsbad is relatively dynamic (see map in Figure 19). The south-western coast of Sandhammaren is subject to statistically significant positive change rates (i.e. erosion), while the south-eastern stretch of the coast shows (statistically not significant) negative change rates (i.e. accretion). Accretion in this area is likely caused by the eastward longshore sediment transport, which advects sediments from the eroding coast further west.

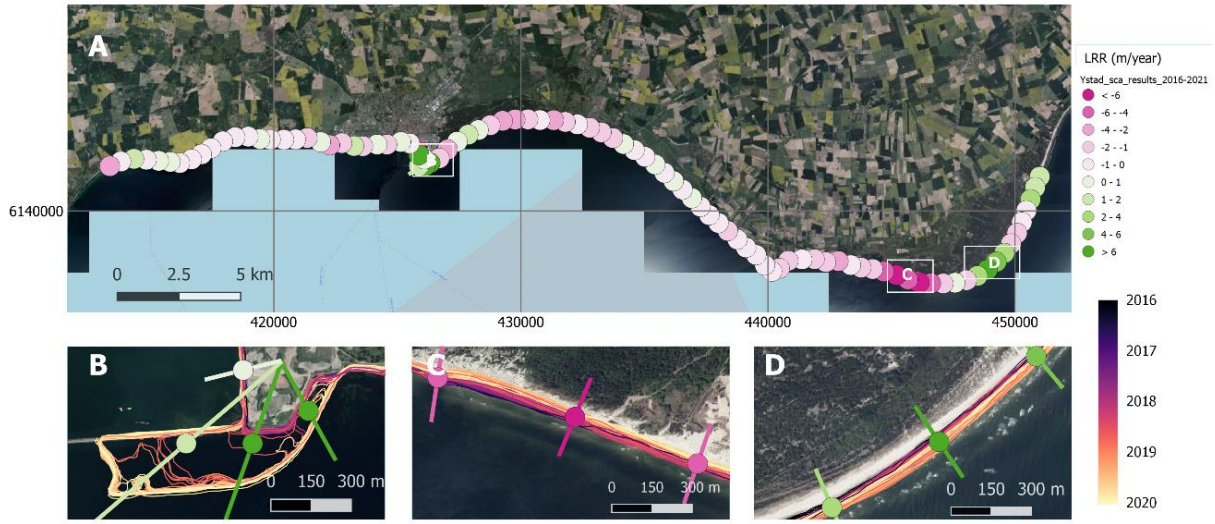

Figure 19: Maps showing the LRR along the coast of Ystad Municipality (A). The small maps in the second row show detailed views of three example regions: Ystad harbour (B), Löderups strandbad (C) and Sandhammaren havsbad (D). The individual shorelines as well as the change rates are shown in more detail.

The following figures show the three subsets from Figure 19 in more detail as well as the time series plots of the shoreline position for one selected transect within the respective region. They showcase the harbour of Ystad (Figure 20), the area of erosion at Löderups strandbad (Figure 21) and an area of accretion at Sandhammaren havsbad (Figure 22). The respective time series plots

show the overall trends of shoreline positions and that there are temporal differences and oscillating evolution of the shoreline positions.

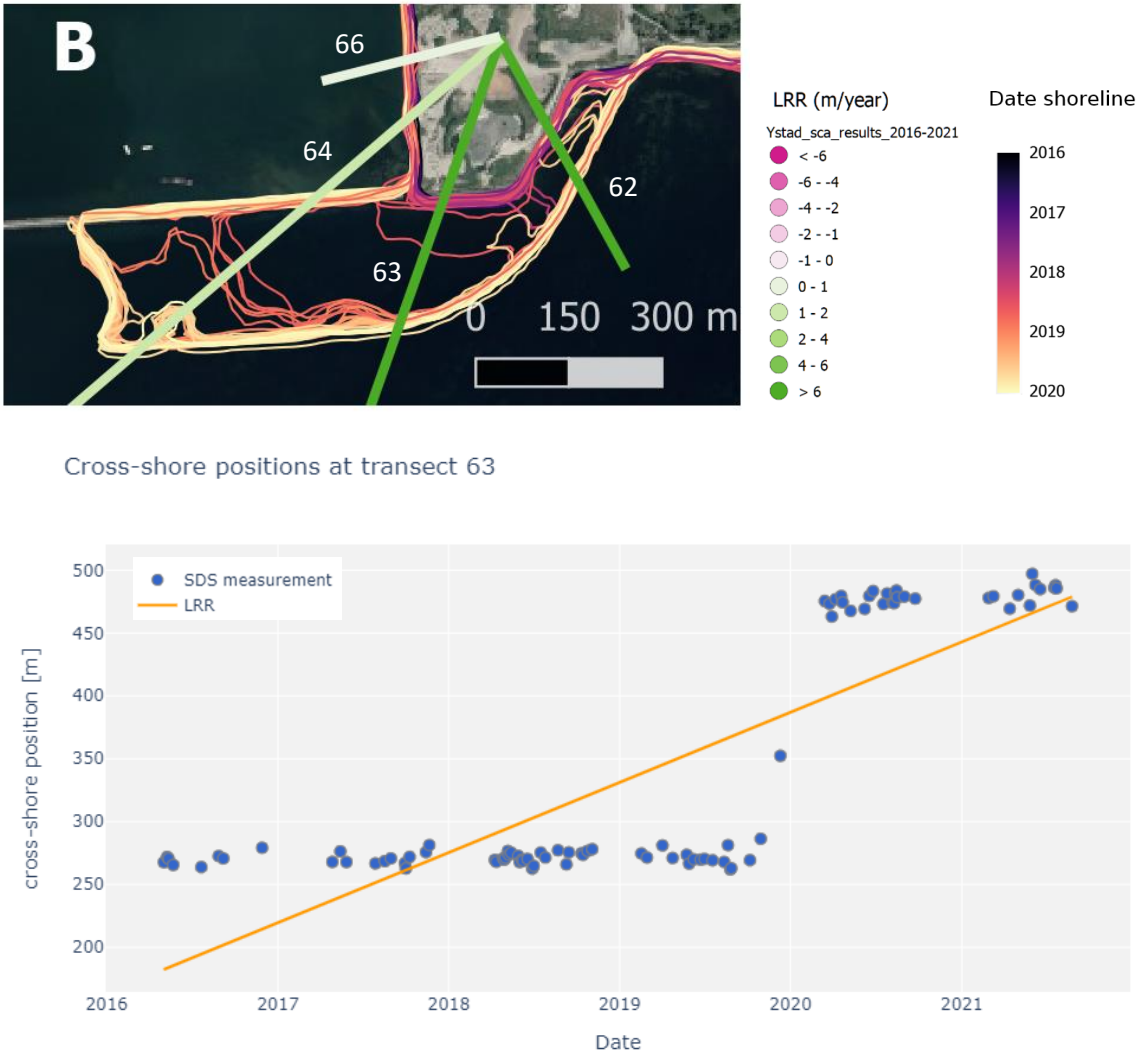

Figure 20: Results of the Shoreline Change Analysis at the harbour of Ystad showing the shorelines for the different years, the Linear Regression Rates (LRR) along the transects. Positive LRRs indicate erosion, while negative values indicate accretion. The scatterplot shows the intersection points of each coastline with transect 63 and the linear regression. The construction period in 2020 can be clearly seen.

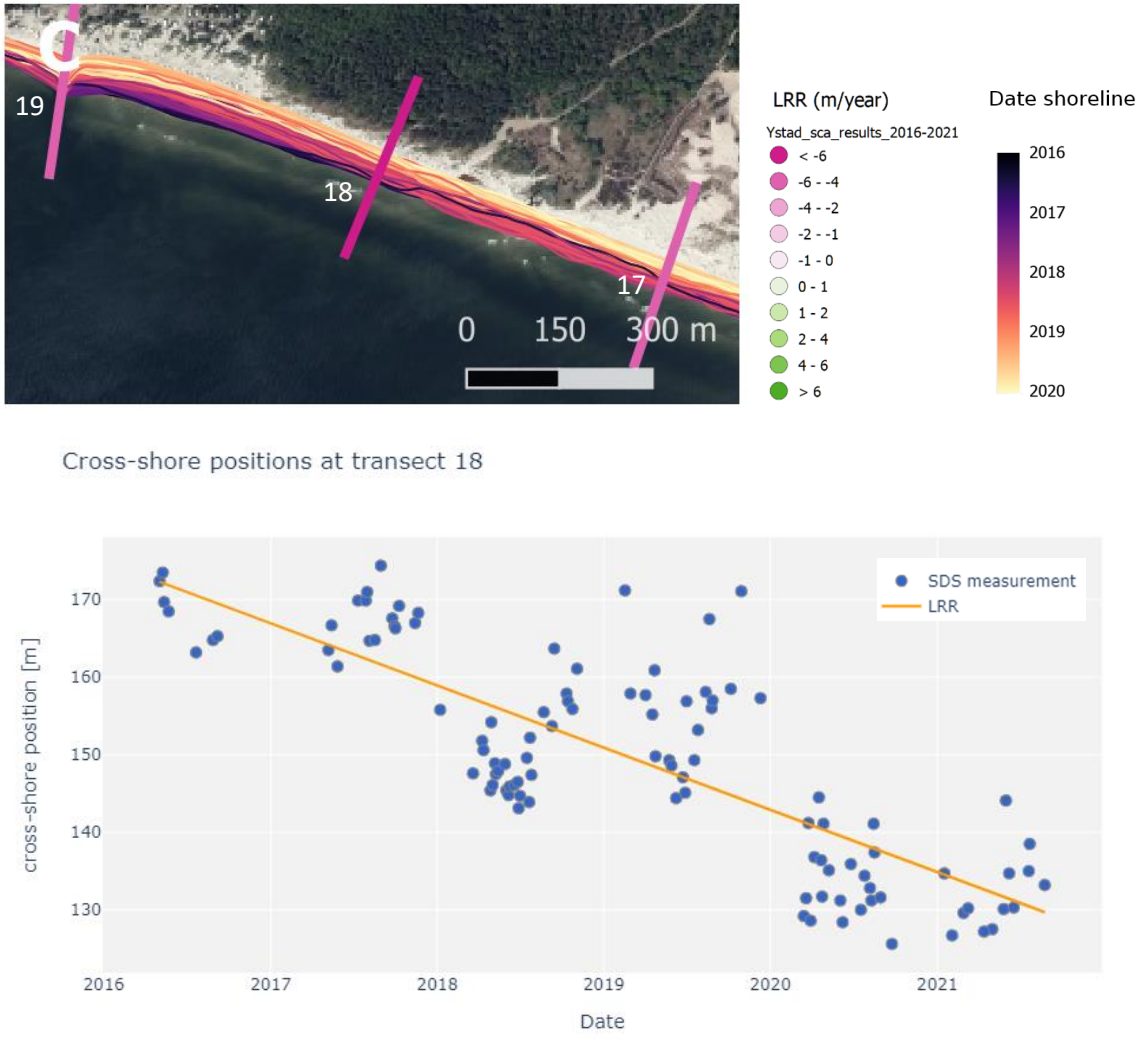

Figure 21: Results of the Shoreline Change Analysis at the east of Löderups strandbad showing the shorelines for the different years, the Linear Regression Rates (LRR) along transects used in this analysis. Positive LRRs indicate accretion, while negative values indicate erosion. The scatterplot shows the intersection points of each coastline with transect 18 and the linear regression.

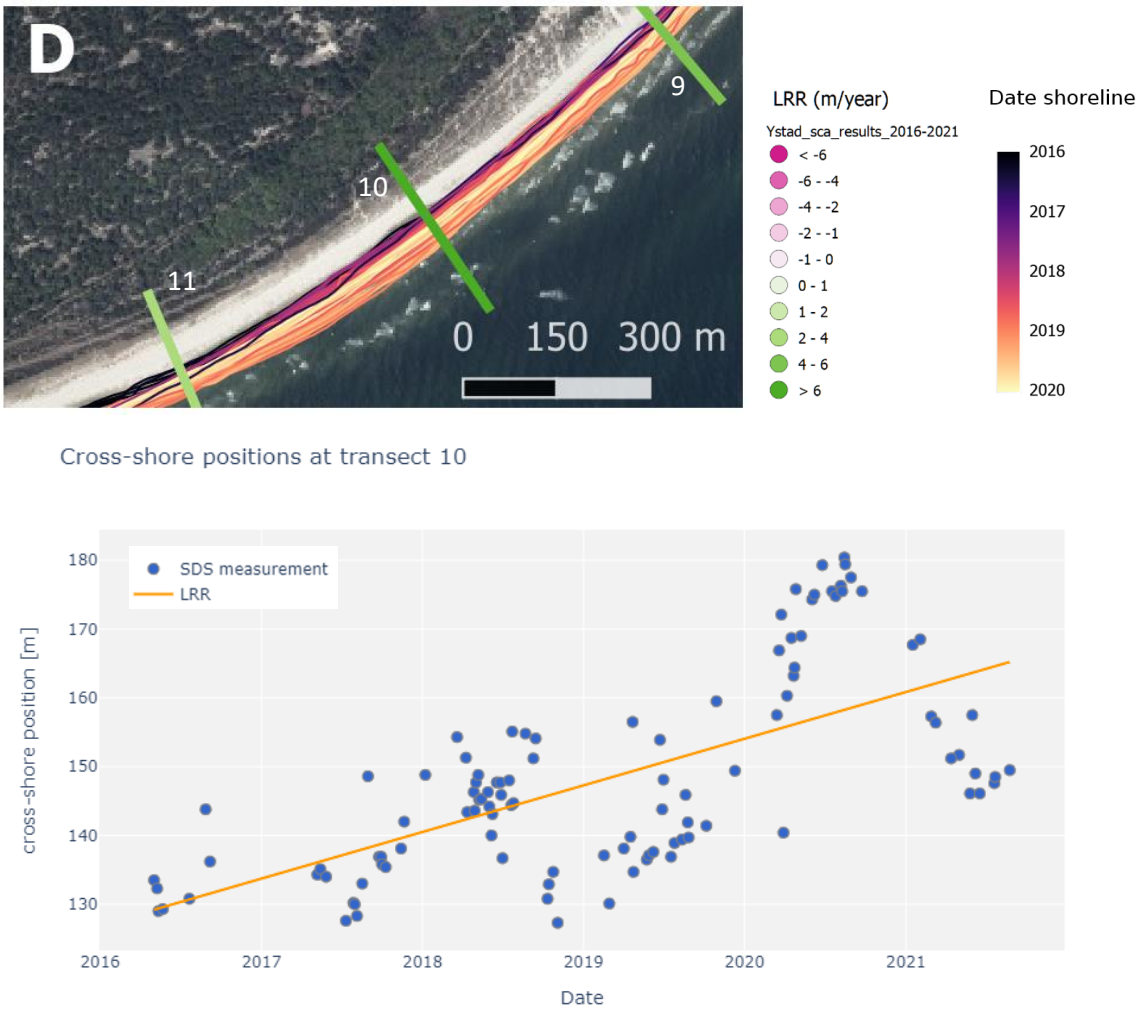

Figure 22: Results of the Shoreline Change Analysis at the at Sandhammaren havsbad showing the shorelines for the different years, the Linear Regression Rates (LRR) along transects used in this analysis. Positive LRRs indicate accretion, while negative values indicate erosion. The scatterplot shows the intersection points of each coastline with transect 10 and the linear regression.

It should be noted that a shoreline that is crossing the transect several times is only registered the first time of crossing. This can lead to misinterpretations in complex shoreline movements as it happens in transect 64 and 69 (harbour construction) and it can happen at river inlets.

5.2 Helsingborg

The changes of the shoreline around Helsingborg are less strong than in Ystad. The LRR ranges from -4 m to 3 m but is mainly between -1 and 1m (Figure 23). The shorelines that are influenced by submerged vegetation or stones during low water occur as outliers in the transect plots as shown for transect 26 in Figure 24. Also, the trend of the shoreline may stay stable over time, but there can be changes in the shoreline position which alter seasonally or irregularly as can be seen in transect 187 (Figure 25).

Figure 23: Change detection for northern and southern parts of the Helsingborg area. Colours indicate the LRR for each transect position in meters.

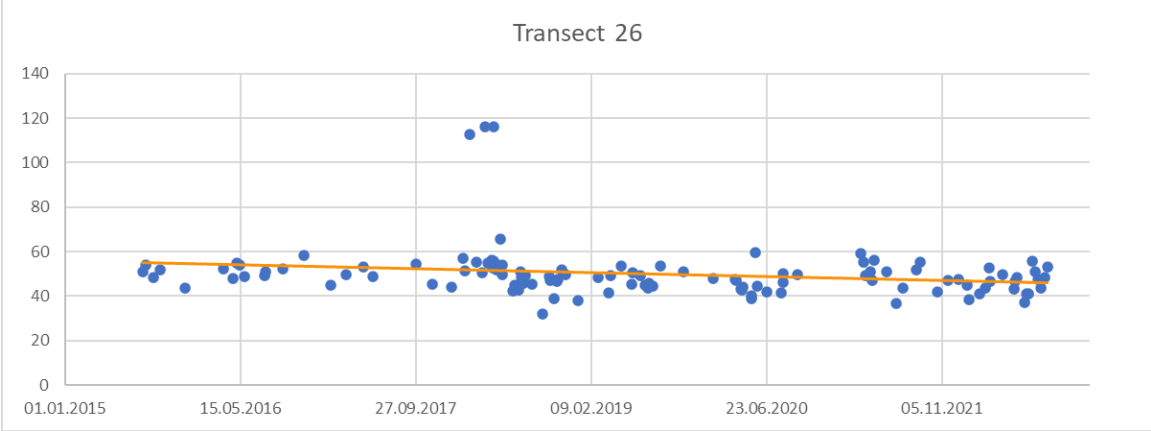

Figure 24: Distance from baseline for Transect 26

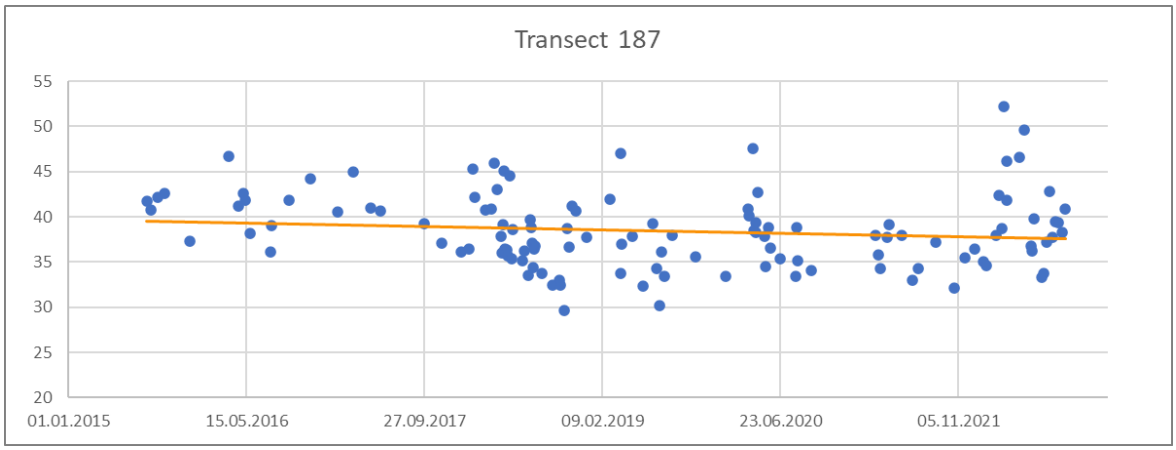

Figure 25: Distance from baseline for Transect 187

5.3 Laholmsbukten

The shoreline change per transect for Laholmsbukten is shown in Figure 26 and Figure 27. Two areas seem to have clear trends, one in the south part of the large bay and one in the northern-central part. Figure 28 and Figure 29 show the transect positions and LRR for two selected transects within the eroded and accreted areas.

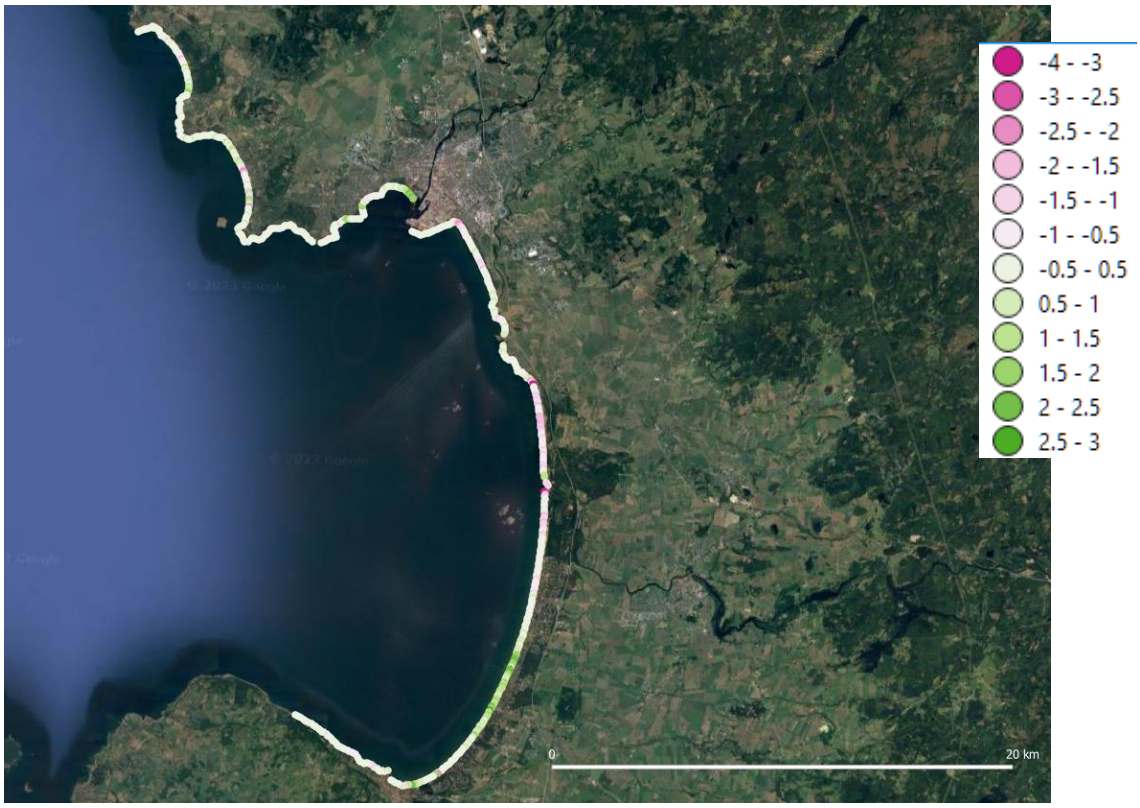

Figure 26: Change Detection (LRR) for Laholmsbukten.

Figure 27: zoom into the coastline change (LRR) for northern and southern part of Laholmsbukten.

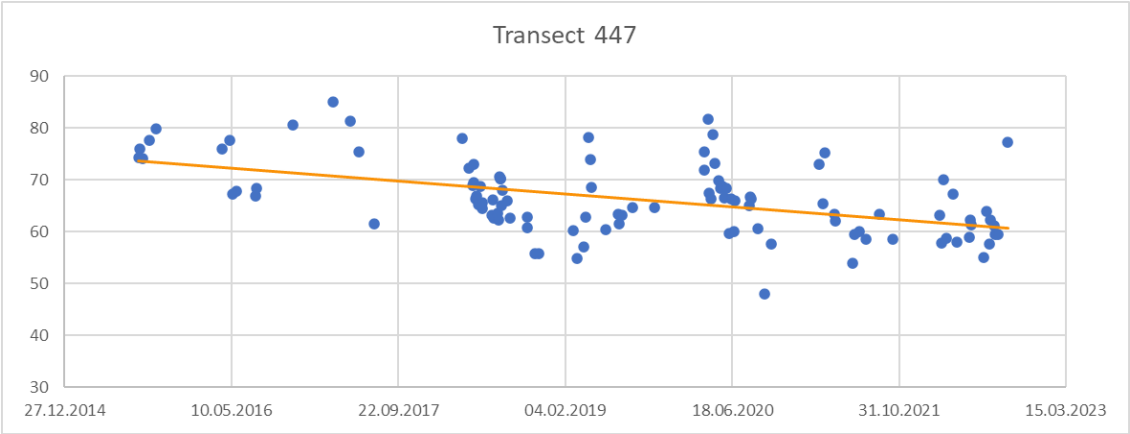

Figure 28: shoreline positions for transect 447

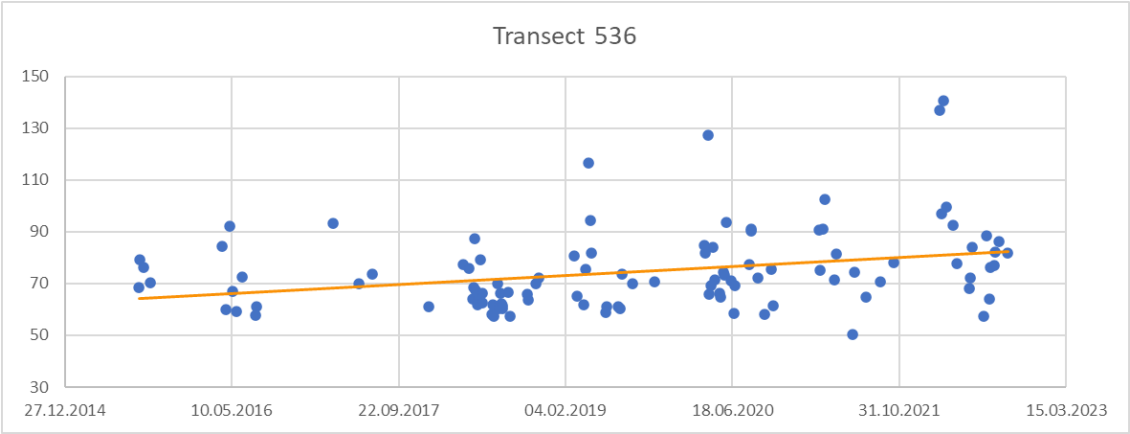

Figure 29: shoreline positions for transect 536

6 Deliverables

With this report, we provide the extracted coastlines and shoreline change analysis for the areas Ystad, Helsingborg and Laholmsbukten. The coastlines are extracted for the years 2015 to 2022 and the shoreline change analysis has been applied for transects every 100m across the coastlines. Each shoreline change analysis data set comes with two vector datasets. One is providing the distance of each single shoreline to the onshore baseline (*_position_*) and the other holds the different statistics for each transect (*_results_*). For the *_results_* shapefiles, two files are provided: one as point vector data set (points located in the middle of each transect), the other as line data set showing the exact position of transects. Both come with the same attributes, to give more options in displaying the results. The coastlines and change information are stored in geojson files. QGIS styles are provided for the shoreline positions and the shoreline change results.

The attribute table of the *_position_* data set holds the position of each shoreline crossing the different transects in meters from the onshore baseline.

The attribute table of the *_results_* data sets hold all SCA measures and statistics. The single attributes are as follows:

NSM	Net Shoreline Movement [m]
SCE	Shoreline Change Envelope [m]
EPR	End Point Rate [m/year]
LRN	number of shorelines used in LRR
LRR	Linear Regression Rate [m/year]
LRI	Intersect of the Linear Regression [m]
LR2	R2 of Linear Regression
LCI	95%-confidence interval of LRR [m/year]
LRP	P-value of test linear regression
LSE	standard error of linear regression

In addition to the geojson files, an html page is provided, which shows the results in an easy way so that no GIS system is needed.

6.1 Ystad

The final delivery for Ystad included the following files provided in the given folder structure:

|- satellite_dervided_shorelines → extracted shorelines from every suitable satellite overpass

- Ystad_201508-202208_satellite_derived_shorelines.geojson

|- shoreline_change_analysis → all results from change analysis

|- 100m

|- positions → position of shoreline for each date for each transect (every 100m)

- Ystad_2015-2022_shoreline_change_analysis_positions_100m_points.geojson

- Ystad_2015-2022_shoreline_change_analysis_positions_100m_transects.geojson

|- results → statistical measures for each transect (every 100m)

- Ystad_2015-2022_shoreline_change_analysis_results_100m_points.geojson

- Ystad_2015-2022_shoreline_change_analysis_results_100m_transects.geojson

- Ystad_2015-2022_shoreline_change_analysis_results_100m.html

- legend_shoreline_change_points.qml

- legend_shoreline_change_transects.qml

6.2 Helsingborg

The structure of the delivered data sets for Helsingorg is as follows:

|- satellite_dervided_shorelines → extracted shorelines from every suitable satellite overpass

- Helsingborg_201508-2022_satellite_derived_shorelines.geojson

|- shoreline_change_analysis → all results from change analysis

|- positions → position of shoreline for each date for each transect (every 100m)

- Helsingborg_2015-2022_shoreline_change_analysis_positions_100m_points.geojson

- Helsingborg_2015-2022_shoreline_change_analysis_positions_100m_transects.geojson

|- results → statistical measures for each transect (every 100m)

- Helsingborg_2015-2022_shoreline_change_analysis_results_100m_points.geojson

- Helsingborg_2015-2022_shoreline_change_analysis_results_100m_transects.geojson

- Helsingborg_2015-2022_shoreline_change_analysis_results_100m.html

- legend_shoreline_change_points.qml

- legend_shoreline_change_transects.qml

6.3 Laholmsbukten

The structure of the delivered data sets for Laholmsbukten is as follows:

|- satellite_dervided_shorelines → extracted shorelines from every suitable satellite overpass

- Laholmsbukten_201508-2022_satellite_derived_shorelines.geojson

|- shoreline_change_analysis → all results from change analysis

|- positions → position of shoreline for each date for each transect (every 100m)

- Laholmsbukten_2015-2022_shoreline_change_analysis_positions_100m_points.geojson
- Laholmsbukten_2015-2022_shoreline_change_analysis_positions_100m_transects.geojson

|- results → statistical measures for each transect (every 100m)

- Laholmsbukten_2015-2022_shoreline_change_analysis_results_100m_points.geojson
- Laholmsbukten_2015-2022_shoreline_change_analysis_results_100m_transects.geojson
- Laholmsbukten_2015-2022_shoreline_change_analysis_results_100m.html
    - legend_shoreline_change_points.qml
    - legend_shoreline_change_transects.qml

7 References

D. Apostolopoulos and K. Nikolakopoulos. A review and meta-analysis of remote sensing data, gis methods, materials and indices used for monitoring the coastline evolution over the last twenty years. European Journal of Remote Sensing, 54(1):240–265, 2021. ISSN 2279-7254. doi: 10.1080/22797254.2021.1904293.

R. Bishop-Taylor, S. Sagar, L. Lymburner, I. Alam, and J. Sixsmith. Sub-pixel waterline extraction: Characterising accuracy and sensitivity to indices and spectra. Remote Sensing, 11(24): 2984, 2019. ISSN 2072-4292. doi: 10.3390/rs11242984.

H. Burningham and M. Fernandez-Nunez. Shoreline change analysis. In D. W. Jackson and A. Short, editors, Sandy Beach Morphodynamics, pages 439–460. Elsevier, London, 2020. doi: 10.1016/B978-0-08-102927-5.00019-9.

B. Castelle, G. Masselink, T. Scott, C. Stokes, A. Konstantinou, V. Marieu, and S. Bujan. Satellite-derived shoreline detection at a high-energy meso-macrotidal beach. Geomorphology, 383(1–4):107707, 2021. ISSN 0169555X. doi: 10.1016/j.geomorph.2021.107707.

M. P. Cipolletti, C. A. Delrieux, G. M. Perillo, and M. Cintia Piccolo. Superresolution border segmentation and measurement in remote sensing images. Computers & Geosciences, 40(28): 87–96, 2012. ISSN 00983004. doi: 10.1016/j.cageo.2011.07.015.

ESA. Sentinel-2 L1C Data Quality Report Issue 71 (January 2022). 2022. URL Quality_Report.

G. L. Feyisa, H. Meilby, R. Fensholt, and S. R. Proud. Automated water extraction index: A new technique for surface water mapping using landsat imagery. Remote Sensing of Environment, 140:23–35, 2014. ISSN 00344257. doi: 10.1016/j.rse.2013.08.029.

J. Heo, J. H. Kim, and J. W. Kim. A new methodology for measuring coastline recession using buffering and non–linear least squares estimation. International Journal of Geographical Information Science, 23(9):1165–1177, 2009. ISSN 1365-8816. doi: 10.1080/13658810802035642.

E. A. Himmelstoss, R. E. Henderson, M. G. Kratzmann, and A. S. Farris. Digital shoreline analysis system (dsas): Version 5.1 user guide: Open-file report 2021–1091, 2021. URL https://doi.org/ 10.3133/ofr20211091.

C. W. Jackson, C. R. Alexander, and D. M. Bush. Application of the ambur r package for spatio-temporal analysis of shoreline change: Jekyll island, georgia, usa. Computers & Geosciences, 41(3):199–207, 2012. ISSN 00983004. doi: 10.1016/j.cageo.2011.08.009.

J. Li, R. Ma, Z. Cao, K. Xue, J. Xiong, M. Hu, and X. Feng. Satellite Detection of Surface Water Extent: A Review of Methodology. Water, 14(7), 2022. doi: 10.3390/w14071148.

S. K. McFeeters. The use of the normalized difference water index (ndwi) in the delineation of open water features. International Journal of Remote Sensing, 17(7):1425–1432, 1996. ISSN 0143-1161. doi: 10.1080/01431169608948714.

P. Philipson, S. Thulin, K. Stelzer, E. Schütt, S. Bokhari Irminger, P. Danielsson, G. Ndayikengurukiye and A. Björlin. Fjärranalysens potential för kustzonsförvaltning. Project report 2021.

D. Scheffler, A. Hollstein, H. Diedrich, K. Segl, and P. Hostert. Arosics: An automated and robust open-source image co-registration software for multi-sensor satellite data. Remote Sensing, 9(7):676, 2017. ISSN 2072-4292. doi: 10.3390/rs9070676.

A. Sekertekin. A survey on global thresholding methods for mapping open water body using sentinel-2 satellite imagery and normalized difference water index. Archives of Computational Methods in Engineering, 28(3):1335–1347, 2021. ISSN 1134-3060. doi: 10.1007/ s11831-020-09416-2.

S. Toure, O. Diop, K. Kpalma, and A. Maiga. Shoreline detection using optical remote sensing: A review. ISPRS International Journal of Geo-Information, 8(2):75, 2019. ISSN 2220-9964. doi: 10.3390/ijgi8020075.

K. Vos, M. D. Harley, K. D. Splinter, J. A. Simmons, and I. L. Turner. Sub-annual to multidecadal shoreline variability from publicly available satellite imagery. Coastal Engineering, 150: 160–174, 2019a. ISSN 03783839. doi: 10.1016/j.coastaleng.2019.04.004.